Seventh International Conference on Computational Fluid Dynamics (ICCFD7), Big Island, Hawaii, July 9-13, 2012

ICCFD7-2006

Design and Evaluation of a Pressure Rail for Sonic Boom Measurement in Wind Tunnels

S. Cliff[1], A. Elmiligui[2], M. Aftosmis[1], S. Thomas[3], J. Morgenstern[4], D. Durston[1]
Corresponding author: Susan.E.Cliff@nasa.gov

[1]NASA Ames Research Center, Moffett Field, CA, 94035, USA
[2]NASA Langley Research Center, Hampton, VA, 23669, USA
[3]Dell Services Federal Government, Moffett Field, CA, 94035, USA
[4]Lockheed Martin Aeronautics, Palmdale, CA, 93599, USA

Abstract: A pressure rail concept for wind tunnel sonic boom measurement of aircraft was manually designed and evaluated with an adjoint-based adaptive Cartesian grid method and validated in various wind tunnel tests. A variety of verification cases requiring the computational modeling of the rail, wind tunnel wall, and test vehicle components predicted the accuracy of the rail concept before manufacture. The rail measures pressure signatures of a wind tunnel model below or at an off-track angle without signature reflection from the surface of the rail or model shocks reflected off the wind tunnel wall. The rail was used in a continuous flow wind tunnel to determine the sonic boom pressure signatures of a low-boom aircraft model with flow-through nacelles and two axisymmetric calibration bodies. The experimental data are compared with computational results with the Cartesian-grid method and two unstructured-grid methods that use tetrahedral cells aligned with the Mach cone angle for improved accuracy. The computed pressure signatures compare well with the experimental data and have provided the incentive for continued rail-based sonic boom testing.

Keywords: Sonic Boom, Pressure Rails, Supersonic, Adjoint, Adaptive Grid.

1 Introduction

Sonic boom minimization is the largest technical hurdle to overcome before worldwide entry of commercial supersonic transports is realized. The Supersonics Project under NASA's Fundamental Aeronautics Program is developing technologies to enable future civilian aircraft to fly efficiently with reduced sonic boom, engine and aircraft noise, and emissions. An objective of the program is to improve both computational and experimental capabilities for design of low boom aircraft. NASA and industry partners are developing improved wind tunnel testing techniques capable of measuring the sonic boom pressure signatures of vehicles with very low overpressure levels. In addition, computational methods are being developed to provide rapid design and analysis of supersonic cruise aircraft with improved meshing techniques that provide efficient, robust, and accurate off-body pressures at several body lengths from vehicles with very low sonic boom overpressures. CFD and experimental techniques are synergistically advancing design and prediction capabilities. An example of CFD advancing experiment will be shown by use of a recently developed CFD technique devised

for accurate analysis of off-body sonic boom pressure signatures. The new CFD method utilizes domain rotation with solution-adapted adjoint methods [1] to evaluate an advanced pressure rail for experimental measurement of low sonic boom pressures associated with modern low-boom aircraft in a wind tunnel. Computational predictions of the accuracy of the new wind tunnel testing equipment are included in this report.

In addition to the development of solution adaptive methods and other techniques that utilize dense meshes within the sonic boom pressure disturbance zone [2-10], highly successful knowledge-based grid generation techniques that utilize Mach cone or Mach angle aligned cells and stretching in the shock-wave propagation direction [11-12] are now being used in design and analysis of vehicles with low overpressures. Domain rotation with an adjoint-based adaptive Cartesian grid method [1], and the Mach cone aligned prism methodology [12] using tetrahedral meshes were chosen for presentation in this report.

Pressure rails for sonic boom testing have been under study at NASA Ames Research Center in the 9-x 7-foot Supersonic Wind Tunnel since 2008 [13]. Pressure rails with hundreds of pressure orifices offer significant gains in efficiency and precision compared to conventional conical probe testing. In 2008, NASA tested two pressures rails with different wall standoff distances and tip cross sections. One of these rails had limited success because of insufficient standoff distance to prevent model pressure signature contamination from reflected shocks off the tunnel wall. In addition, the curved cross-sectional shapes of both rails partially reflect the model's signature resulting in variable reflection factors over the length of the pressure signature. Historically, needle-like 2-degree conical probes were used to measure the static pressures in the model flow field and required 40-60 minutes to acquire a complete pressure signature. Each point on a sonic boom signature is obtained one at a time when conventional single probes are used, whereas pressure rails measure all pressures simultaneously for a single model position and produce an entire model signature in seconds.

The new pressure rail was used in the Ames 9 x 7-foot Supersonic Wind Tunnel (test T97-0231) in 2011 during phase I of a NASA Research Announcement contract with Lockheed Martin Aeronautics Company. The contract is managed by the NASA Supersonics Project and is part of the Supersonics Validation Program, in which second-generation "N+2" supersonic vehicles are being designed and evaluated for projected entry into service in 2020. The test was conducted jointly with Lockheed Martin (LM) using N+2 models of supersonic aircraft that were designed to address environmental and performance goals specified in the NASA Research Announcement. The models represent vehicles designed for low sonic boom loudness levels and high cruise efficiency. Two axisymmetric calibration models were also tested during the October 2011 test entry, one designed and manufactured by The Boeing Company and the other by Lockheed Martin.

2 Objectives, Design, and Description of Pressure Rail Instrumentation

Pressure probes that measure a single model pressure require axial translation of the test vehicle past the probe using a move-pause data acquisition method. The accuracy of the data obtained with probes can be compromised by changes in tunnel flow conditions during the 40-60 minute data acquisition times. Wind tunnel humidity and pressure variations over time and model lift changes due to translation through varying tunnel stream angles are common during the long data-acquisition times. In addition, the model experiences pressure variations from ambient tunnel shock waves and expansion regions over the length of the traverse.

At the time the rail was conceptualized, industry (Boeing and Lockheed) was focused on rails or pressure plates that would perfectly reflect the pressure signature, with reflection factors of 2.0. The concept of a non-reflective, reflection factor (RF) 1.0, rail can be envisioned by recalling that the single conical probe measures the static pressures along the side of the cone. Figure 1 shows an illustration of the model bow shock passing over the static pressure orifice of a 2-degree pressure

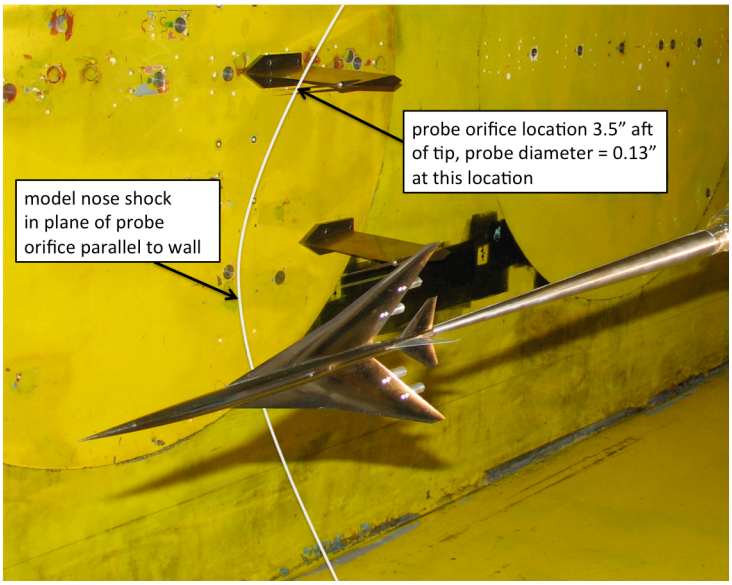

Figure 1: Illustration of the model bow shock Mach cone intersecting the plane of the probe with shock striking the upper overpressure probe at the single static pressure orifice on the side of the probe.

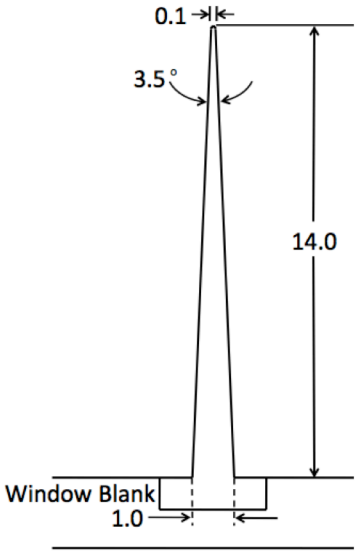

Figure 2: Cross section of the rail with dimensions in inches.

the pressure-measuring section and reattached to the aft end of the extension. Budget constraints made it prudent to manufacture only one of the two pressure measuring portions of the long rail. The rail stands off the wall 14 inches, has a 0.05-inch radius tip, and a 1-inch base width.

probe. The model is mounted wings-vertical in the Ames 9x7 tunnel with probes mounted on the sidewall. A pressure rail with a rounded tip diameter equivalent to that of a pressure probe at the static pressure port was thought to permit three-dimensional flow similar to the side of the cone probe. Also a very thin blade-like rail with a small 3.5-degree angle from the tip to the base (Figure 2) was thought to be shallow enough to avoid shock reflection.

A CAD drawing of the RF 1.0 rail design is shown in Figure 3. The rail is shown attached to two window blanks (flat circular steel plates that replace the windows in the 9x7 wind tunnel) in the CAD drawing. The window blanks were manufactured with slots to allow the pressure tubing to pass from the interior to the exterior of the tunnel. The rail is comprised of three sections: leading, trailing and center. The trailing edge piece can be removed to extend the length of

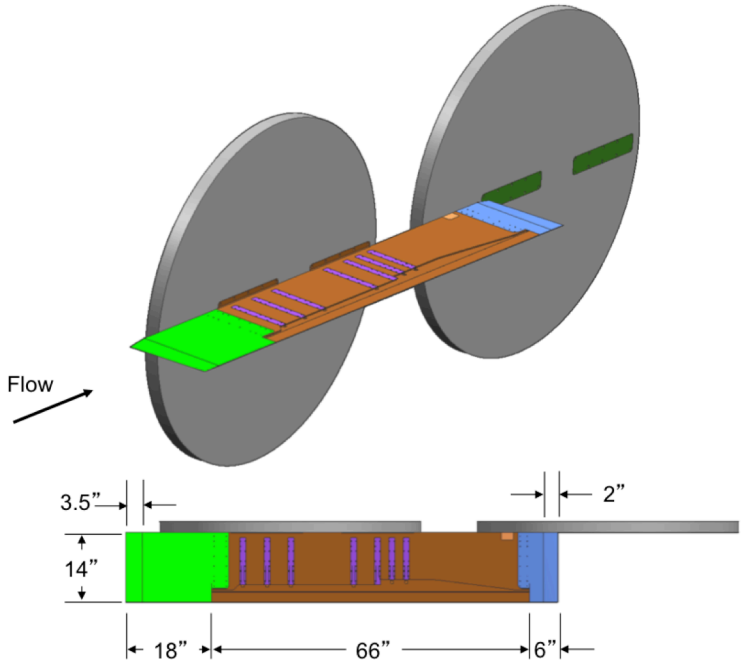

Figure 3: Isometric and top views of the RF 1.0 rail.

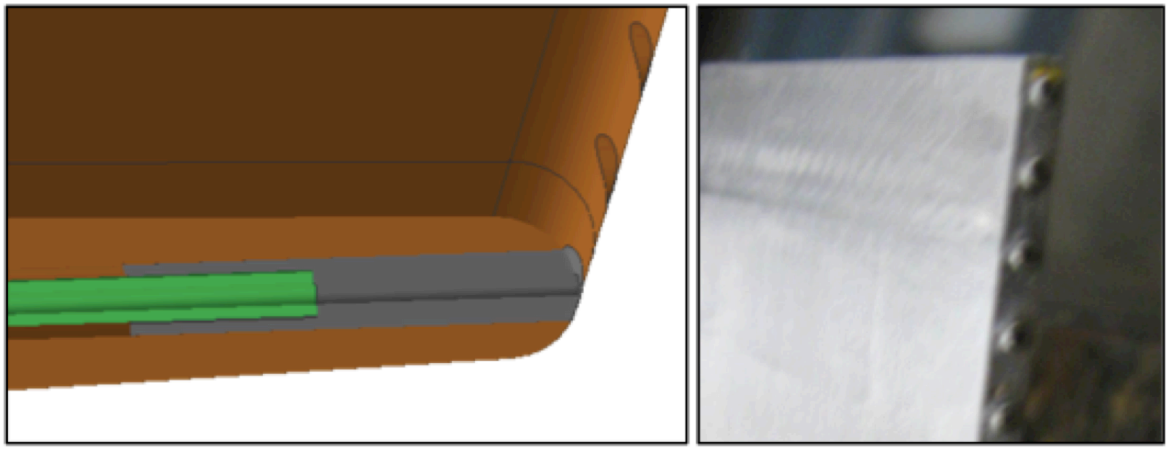

Figure 4: CAD and manufacturing details of the pressure orifice design of the rail tip. Cross-sectional view of the ferrule is shown in gray and pressure tubing in green in the CAD illustration. Ferrules are installed in the rail tip prior to machining of the round tip in the photograph.

Figure 5: Photograph of the RF 1.0 rail showing the routing of 420 metal pressure tubes channeled through machined grooves on one surface of the rail.

The rail height was selected to prevent the reflected model shock waves from affecting the pressure signature orifices on the rail. The 14-inch height was determined by Lockheed to provide reflection-free data for expected model sizes and test Mach numbers of interest. A maximum model length of 35 and 43 inches can be tested at Mach 1.6 and 1.8, respectively, without contamination from shocks reflected off the wall. Ferrules were installed in the tip of the rail (Figure 4) with 0.015-inch diameter orifices placed 0.16 inches (4 mm) apart. Metal pressure tubing (green) attaches to the ferrules (gray) as shown in the cross-section image on the left in the figure. The installed ferrules shown in the photograph of the rail during fabrication are on the right prior to machining of its rounded tip shown on the left. The metal pressure tubing was routed through grooves on one side of the rail as shown in Figure 5. A total of 420 pressure tubes are routed through the seven grooves shown in purple in the CAD drawing in Figure 3 and in the photograph in Figure 5.

Figure 6 shows an installation photograph of the rail mounted on the forward window blank on the wall of the 9x7 wind tunnel. The LM N+2 model is rolled with wings vertical for sonic boom measurement below the model with the RF 1.0 pressure rail.

Figure 6: Photograph of the RF 1.0 rail attached to the forward window blank in the 9x7 Wind Tunnel.

The design attributes of the RF 1.0 rail are the following:

- Consistent reflection factor of 1.0 (no scaling of the data is required)
- Small circular radius tip permits three-dimensional flow (smaller diameter than conventional probe at orifice location)
- Model shocks reflect from the wall downstream of measured signatures and hence do not corrupt signatures (for aforementioned model sizes and Mach numbers)
- Rail has a weaker leading shock/compression region compared with conventional pressure rails and plates resulting in minimal impact on signature accuracy if model is behind or translated through the shock
- Pressures are measured outside the tunnel boundary layer. No Mach differential between rail and model is present

Rail-based sonic boom testing reduces the data acquisition time and allows for the model flow field to be measured at one model position in the tunnel. However, use of a pressure rail does not eliminate errors caused by ambient tunnel shocks and expansions, but these tunnel distortions can be reduced or eliminated by spatial averaging of the data with the model at multiple tunnel positions. Ideally, the model traverse distance spans the flow field variation cycle in the wind tunnel. Spatial averaging causes only a minor loss in productivity because preliminary data analyses indicate that the number of model positions, and the time to obtain each pressure signature at each model position can be reduced with little effect on the data quality of the averaged signatures.

The RF 1.0 rail concept is very different from a 2-degree conical pressure probe or conventional pressure rails, necessitating CFD computations to understand the flow-field characteristics of the rail mounted on a simulated wall of the wind tunnel with and without model sonic boom pressure influence. To address these differences, the new rail concept underwent extensive evaluation with

computational simulations. An adaptive grid approach is ideally suited for validation of the concept since solutions naturally offer the optimal number and distribution of grid points with the least computational error.

3 Computational Results for Pressure Rail

The RF 1.0 rail concept was evaluated with CFD before NASA and Boeing approved the design for manufacturing. CART3D [5-7, 9, 15] in conjunction with the Adjoint Error Optimization (AERO) module was used to provide simulations of a "Seeb" body of revolution wind tunnel test model, the RF 1.0 rail, and the wind tunnel wall. The "Seeb-ALR" (aft lift relaxation) axisymmetric body was designed by Lockheed utilizing the work of Seebass, George and Darden [16-17] for a low-boom low-drag body with modification to relax the aft lift requirements. The initial computational simulation was with the model offset 50 inches downstream of the rail leading edge, and at an altitude of one body length from the rail at H=17.68 inches. This places the Seeb-ALR behind the compression region of the rail leading edge. The computational result of the Seeb-ALR, RF 1.0 rail, and tunnel wall is shown in Figure 7. The model's leading shock reflects from the wall far downstream of the

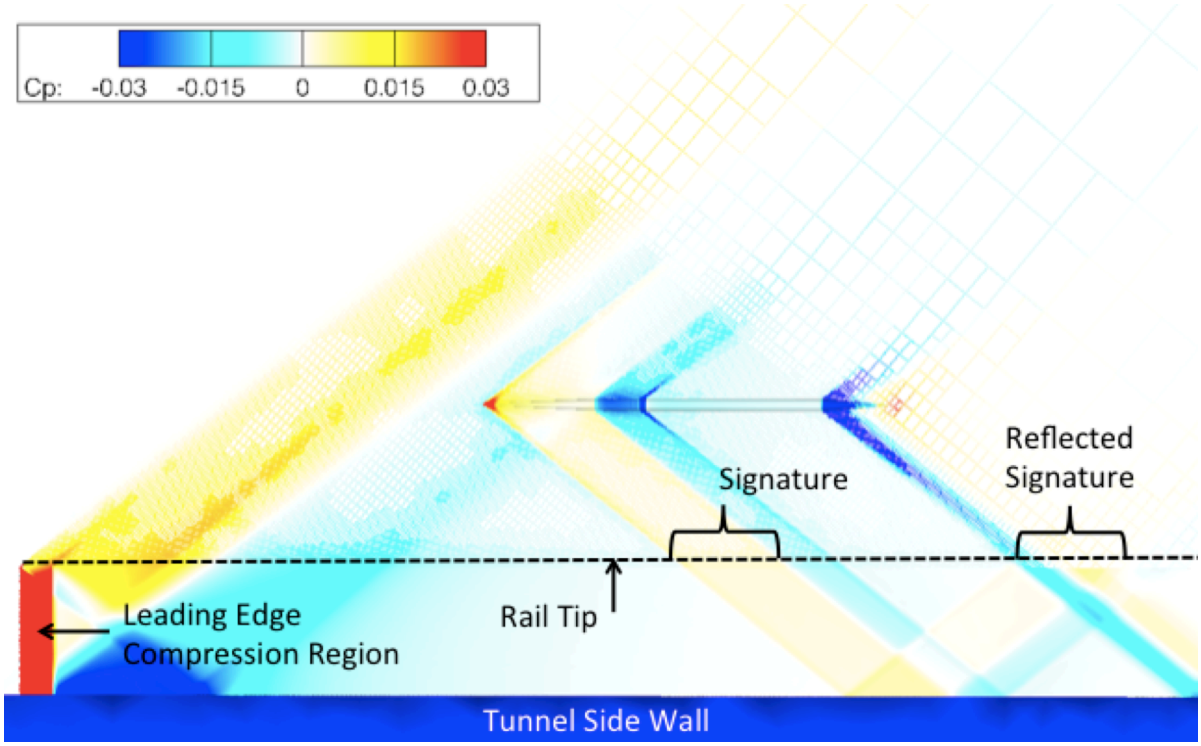

Figure 7: CART3D-AERO simulation of the Seeb-ALR, RF 1.0 rail, and wall. M=1.6, α=0.0 deg, H=17.68.

model pressure signature on the rail. The computation utilizes mesh adaptation that seeks to minimize error along a line sensor placed 0.1 inches above the tip of the RF 1.0 rail. The entire domain is rotated at the Mach angle (offset 1.0 degree to avoid minor oscillations in the computations associated with perfect alignment). Aligning the mesh near the Mach angle is important even for mesh adaptation methods to reduce the effects of dissipation in the solutions and to obtain accurate solutions with reasonable computational cost. The symmetry plane mesh colored by the pressure coefficient is shown as well as the pressures on the rail, model and wall in the figure. Two additional computations were run with line sensors in the same position: first the rail and wall computation without model, and then the Seeb-ALR in free air (without the rail and wall). The pressure signature along the line sensors are extracted from the three solutions and plotted in Figure 8a. Subtracting the

rail and wall solution from the Seeb-ALR, rail, and wall computation yields the sonic boom pressure signature of the vehicle. The result compared with the free-air computation is shown in Figure 8b. Little difference in the computations shows that the RF 1.0 rail provides a good pressure rail design without any indication of reflection from the rail.

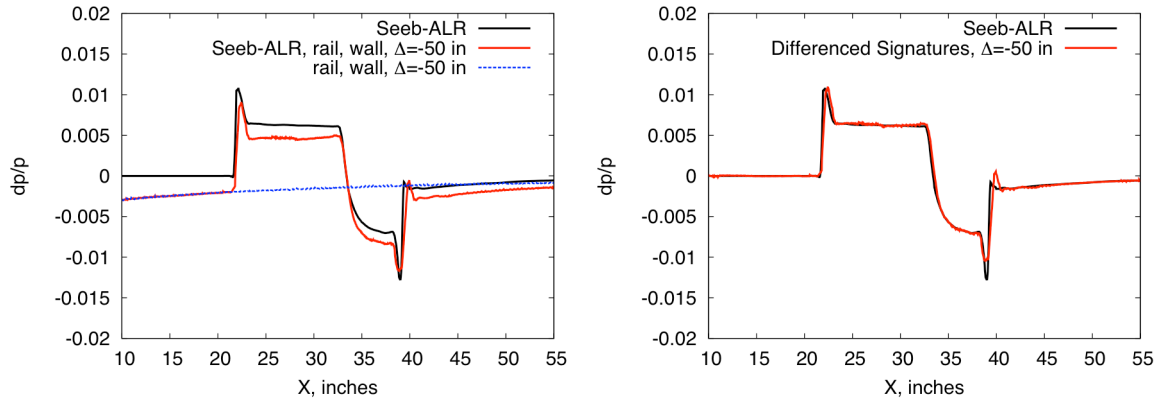

a) Seeb-ALR, RF 1.0 rail, and tunnel wall b) Predicted signatures of RF 1.0 rail

Figure 8: CART3D-AERO computations of Seeb-ALR, RF 1.0 rail, and tunnel wall. Pressure signatures at line sensor located one body length (H=17.68 in.) below model with the rail leading edge Δ=−50 inches from the model nose. M=1.6, α=0.0 deg.

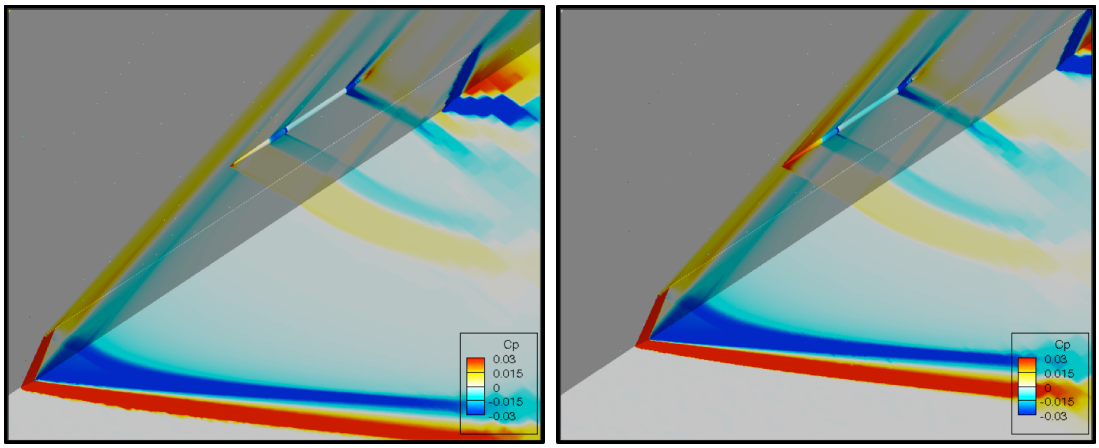

a) Δ=−50 inches b) Δ=−30 inches

c) Δ=−20 inches d) Δ=−10 inches.

Figure 9: CART3D-AERO evaluations of Seeb-ALR passing through rail leading edge shocks for rail axial displacements of Δ=−50, −30, −20 and −10 inches. M=1.6, α=0.0 deg.

The RF 1.0 rail was evaluated for a series of simulated model translations that pass the model through the leading shock of the rail. Computations at axial displacements Δ=–10, –15, –20, –25, –30, and –35 inches were performed. Results of the –10, –20, –30 and –50 displacements are presented in Figure 9. These images are rotated so that the tunnel wall is displayed below the rail. The symmetry plane of the rail is colored by Cp, showing the shocks from the rail leading edge as well as the shocks from the Seeb-ALR body. The model passes through the compression region emanating from the rail leading edge in the computations at Δ=–30 and –20, and the model (forward conical body) is upstream of the shock region at the –10 displacement position. The pressure signatures of the Seeb-ALR, rail, and wall, and the rail and wall computations are plotted in Figure 10 for Δ= –30, –20 and –10. Two effects are being evaluated in the computations: the effect of more aged model shocks

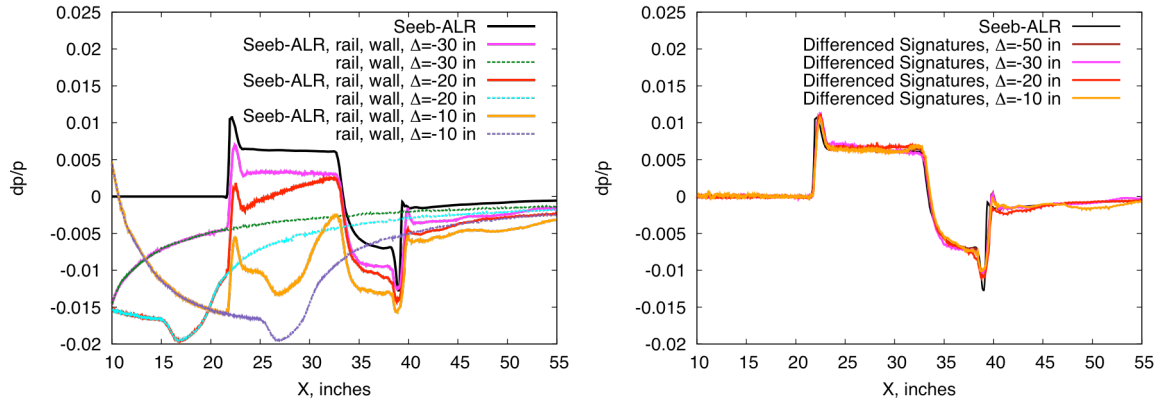

a) Seeb-ALR, RF 1.0 rail, and tunnel wall pressure signatures

b) Differenced signatures compared to model free-air solution

Figure 10: CART3D-AERO pressure signatures at line sensors located one body length (H=17.68 in.) below model for combinations of Seeb-ALR, rail, and wall components with the rail leading edge Δ=–30, –20, and –10 inches from the model nose. M=1.6, α=0.0 deg.

passing through less aged (stronger) rail shocks as the model/rail axial separation decreases, and the rail shocks effect on the model pressure signatures. The computational results shown in Figure 10b indicate that the rail is successful in both situations. It was thought that the weak model shock passing through a stronger rail shock might distort the model shocks with a corresponding pressure effect, but no evidence of this is observed. The rail shock region striking the model is expected to have an effect on a lifting model, however.

Computations with the rail shock region striking the LM N+2 aircraft model were compared with solutions with the rail shock behind the model using CART3D-AERO. The result with the rail leading edge 12.61 inches ahead of the model nose and height H=21.2 is shown beside a solution with the rail leading edge 6 inches behind the model nose in Figure 11. The rail positioned 12.61 inches upstream of the model causes the rail shock to strike the model (Fig. 11a), whereas shock impingement does not occur with the rail placed 6.0 inches downstream of the model (Fig. 11b). Figure 12 shows the computational results of the model, rail and wall at the two different rail positions, and the two rail and wall solutions, as well as the free-air solution of the LM N+2 model at M=1.6 α=2.3 deg. The computed pressure signatures that occur with the different rail positions are compared with a free air solution in Figure 12a. The compression region emanating from the rail leading edge affects the pressure signatures when model impact occurs. The modest change in pressures occurs in the region of the pressure disturbance (Fig. 12b). This effect may be small when averaging the experimental pressure signatures taken at several axial positions but should be avoided when possible.

The LM N+2 model was purposely passed through the rail leading edge shock to evaluate this effect experimentally in a diagnostic wind tunnel test (T97-0250) in April 2012. The data sampling time

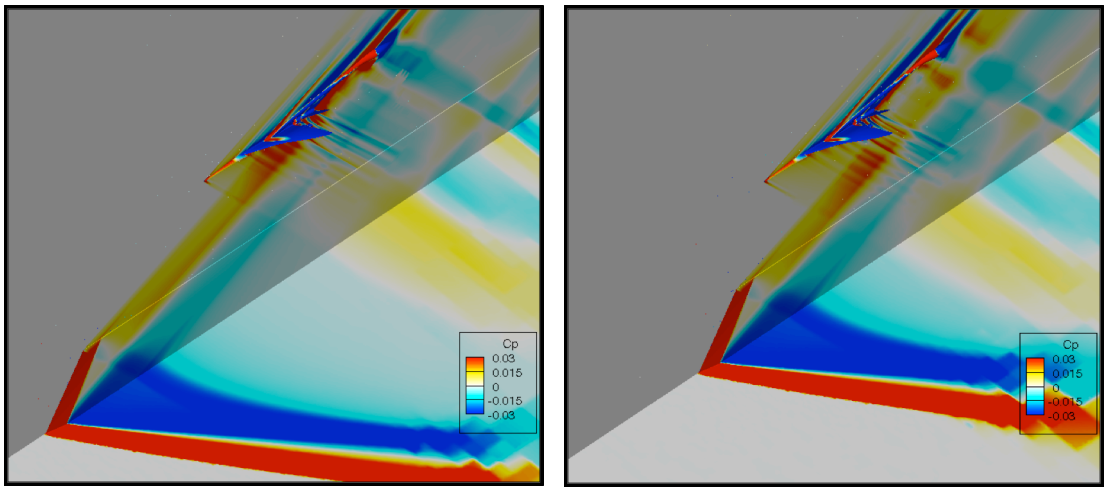

a) Δ=−12.61 inches b) Δ=6.00 inches

Figure 11: CART3D-AERO evaluations of LM N+2 blade sting with rail leading edge shocks striking model and upstream of shocks, M=1.6, α=2.3 deg.

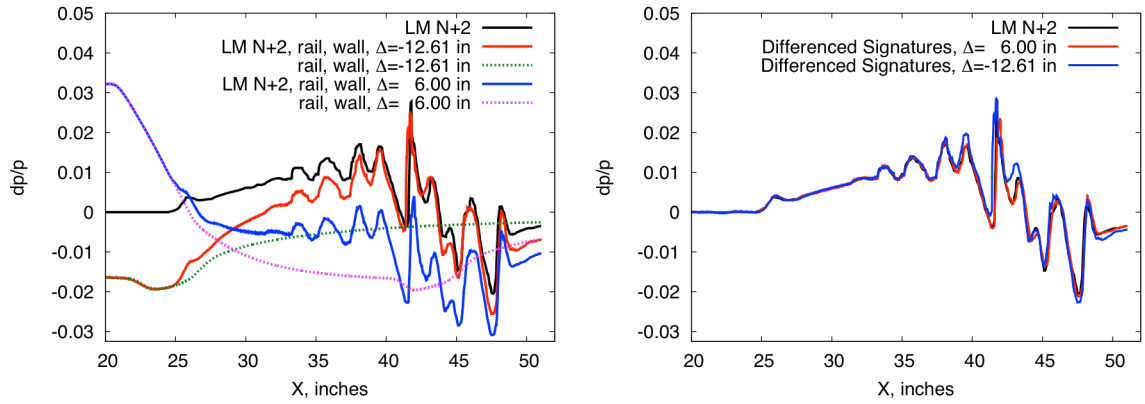

a) LM N+2 blade mount, RF 1.0 rail, and tunnel wall pressure signatures

b) Differenced signatures compared with model free-air solution

Figure 12: CART3D-AERO computations of LM N+2 blade mount, RF 1.0 rail, and tunnel wall Rail shock strikes model at axial displacement Δ=−12.61 inches and is aft of model at Δ=6.0 inches. M=1.6 α=2.3 deg, H=21.2 inches.

during this test was only 10 seconds, compared with 30 or 60 seconds used during the T97-0231 test which results in greater oscillation and poorer signature quality at fixed model positions in the tunnel. In spite of the data quality, there appears to be an effect from the rail leading edge shock impacting the model that is similar to the predicted results (Figure 13).

The model was positioned upstream of the rail leading edge shock and significantly longer data sampling times were used for each run or model position in the tunnel during test T97-0231. The data from T97-0231 are presented in the remaining sections of this report.

The rail was also evaluated in a 1.0 degree cross flow condition with the Seeb-ALR axisymmetric body with the rail displaced axially −15 inches from the model nose—about the least favorable position for the rail shock impact on the model. The isometric view of the solution in Figure 14 shows asymmetric pressures on the wall with the leeward side of the rail facing the viewer, and the model in the midst of the rail compression region (compare with Figure 9). The transparent symmetry plane allows the pressure coefficient on both sides of the wall to be visible in the computational results.

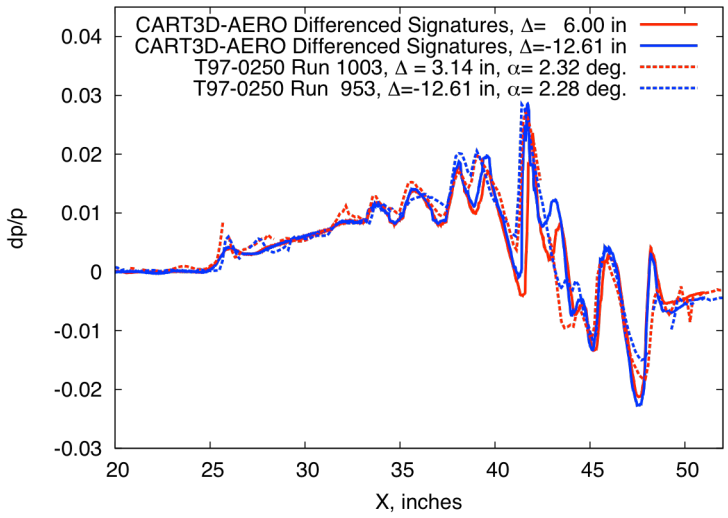

Figure 13: Experimental data (T97-0250) for N+2 model with (Run 953, Δ=−12.61) and without (Run 1003, Δ=3.14) rail shock impact on model, compared with CART3D-AERO computations with (Δ=−12.61) and without (Δ=6.0) rail shock impact.

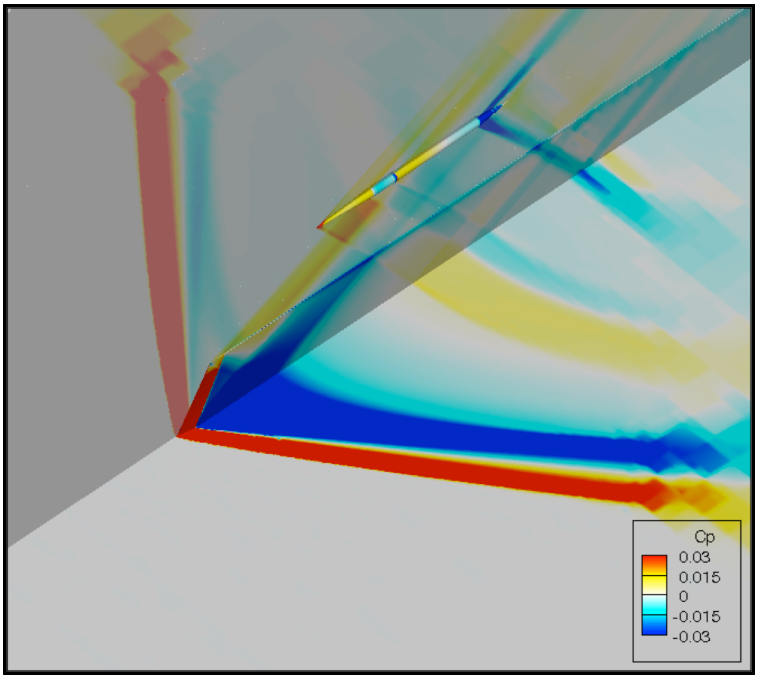

Figure 14: CART3D-AERO evaluations of rail in cross-flow with rail leading edge shock impact on model, rail axial displacement of Δ=−15 inches. M=1.6, α=0.0 deg, β=1.0 deg, H=17.68 inches.

Wind tunnel calibration data indicate a ±0.3 degree stream angle variation in the 9x7 tunnel in the vertical and horizontal planes. The lack of cross-flow effect provided evidence that small changes in tunnel cross-flow (beta stream angle) should not affect the accuracy of the RF 1.0 rail data. The pressure signatures extracted from the flow fields along line-sensors located very near the rail tip for the three computations are shown in Figure 15a. The resultant computations show that even with the analyses of greater cross flow than expected in the wind tunnel there isn't any evidence that this will affect the accuracy of the rail data (Figure 15b). The small oscillations in the computational signatures are a result of discretization errors, and are associated with the line sensor proximity to the very small radius tip of the rail. These are not problematic and slowly diminish with additional adaptation cycles.

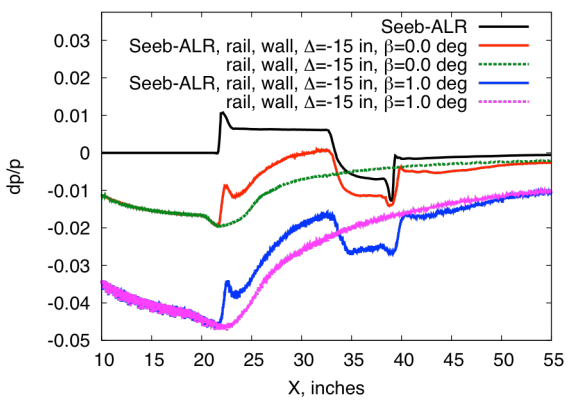

a) Pressure signatures with and without cross flow, and with rail shock striking model

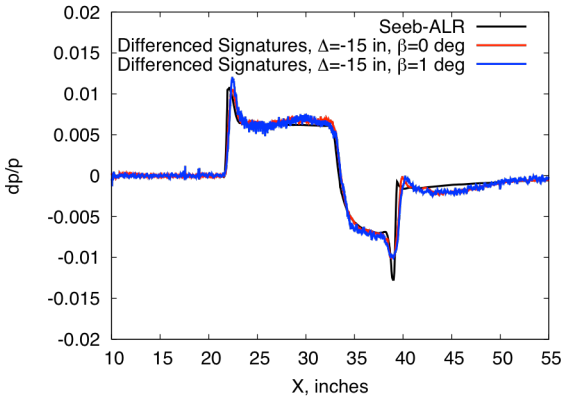

b) Differenced signature with and without cross flow

Figure 15: CART3D-AERO predicted pressure signatures with and without 1-degree cross flow. Rail displaced Δ=–15 inches to place model in midst of rail shock. M=1.6, α=0.0 deg, H=17.68 in.

4 Wind Tunnel Testing Techniques and Spatial Averaging

The installation photograph previously shown in Figure 6 depicts the RF 1.0 rail in the forward position, mounted on the upstream window blank in the 9x7 wind tunnel. The LM N+2 model is attached to a highly swept blade model support on the top of the fuselage that connects to the wind tunnel support hardware. The linear actuator, aft of the blade model support, is used to translate the model axially in the tunnel, and the strut is used to translate the model laterally in the wind tunnel to change the distance between the model and the rail (altitude). The strut centerbody sets the angle of attack or sideslip downstream of the model support and linear actuator. Sandwiched between the linear actuator and strut centerbody is a roll mechanism that is used to acquire off-track pressure signatures.

Obtaining accurate sonic boom data for a model with very weak overpressures is difficult in a wind tunnel. The wind tunnel flow is turbulent and unsteady, causing model oscillations and rounding of the measured pressure signatures. The tunnel test section has stream angle variations of about a third of a degree over distances of only 5 inches of axial distance resulting in lift coefficient changes of approximately 0.015 during model traverses. In addition, the low sonic boom configurations of interest today have pressure waves that are mostly weaker than the magnitude of the tunnel (empty) ambient wavelets. The ambient tunnel pressure waves observed in Schlieren images randomly shift position over distances on the order of one-quarter inch on average (Figure 16). Limited optical access with

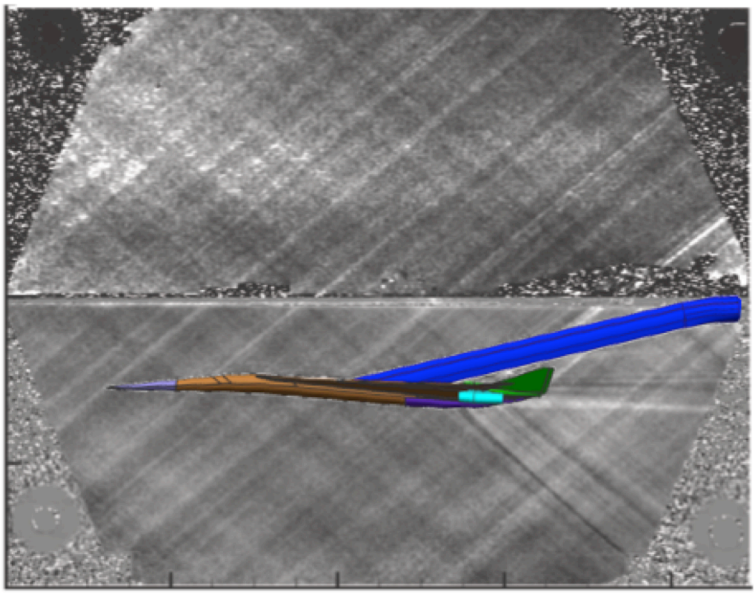

Figure 16. Retroreflective background oriented Schlieren image of LM N+2 model with blade mount, and RF 1.0 rail (centered vertically) in 9x7 wind tunnel. M=1.6. Model superimposed.

sonic boom testing required retroreflective background oriented Schlieren techniques [18] using reflective material attached to the window blank to obtain the image shown in the figure. A colored model is superimposed to clarify the position of the model in the image.

NASA and its industry partners, Lockheed Martin and The Boeing Company, have been focused on finding improved testing techniques to improve the accuracy and efficiency with which sonic boom data can be obtained and have been evaluating several pressure rail designs since 2008. The rail with a row of 420 pressure taps measures a complete signature for one model axial position. However, a reference run, with the model moved away from the pressure signature zone of influence of the data run, is necessary. Figure 17 shows the procedure used to obtain experimental pressure signatures with

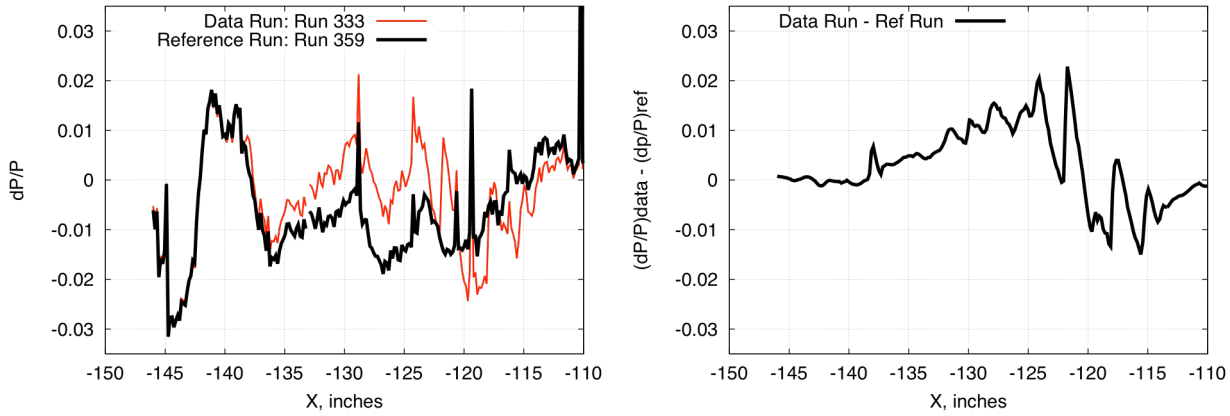

a) Uncorrected pressure signatures for data and reference runs.

b) Resultant pressure signature from differenced reference run from data run.

Figure 17: Pressure rail data acquisition method.

rail instrumentation. The data in Figure 17a use the tunnel static pressure as the free-stream value in the standard definition of $dp/p = (P_{rail} - P_\infty)/P_\infty$. Note the magnitude and oscillatory nature of pressures measured on the rail; this is an indication of the irregular tunnel ambient flow field. The corrected pressure signature of the model is obtained by subtracting the reference signature from the data signature, as shown in Figure 17b.

NASA and Lockheed Martin employed several testing techniques in an attempt to improve the accuracy of the data. Listed below are some of the techniques explored:

- Spatially average the data at constant H/L
- Operate the tunnel at P_T (total pressure) of 2300 psf and maintain within 1 psf
- Reduce the humidity to approximately 230 ppm and maintain within 4 ppm
- Obtain data with the RF 1.0 rail in the forward tunnel position
- Position the model upstream of the leading edge shocks from the RF 1.0 rail
- Increase the model size for a greater signal to noise ratio
- Increase the duration of the reference and data runs

4.1 Spatial Averaging

A spatial averaging technique was developed using the T97-0231 test data [19-20]. Pressure signatures at 26 axial positions were averaged to reduce the effect of tunnel flow field distortions on the data at fixed axial locations. Figure 18 shows the model translations and travel distances for the two altitudes used in this test. For the smaller altitude data only 4 inches of model travel was used to keep the model upstream of the rail leading shocks. With the model 21.2 inches from the rail, the model was translated forward 1 orifice at a time, equating to 4 mm or 0.16 inch travel. This represents the minimum model translation for spatial averaging, and results in a series of 26 model positions

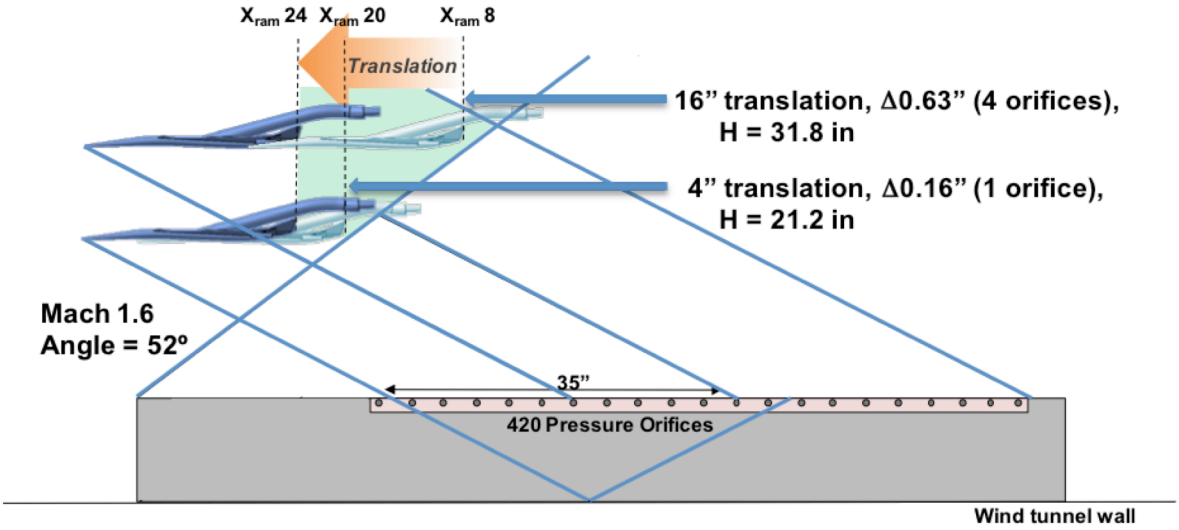

Figure 18: Model and rail positioning for the two translation series at test altitudes, H=21.2 and 31.8 inches at Mach 1.6.

over the 4-inch traverse. A 4-inch traverse may not be enough to capture an entire cycle of the flow-field distortions in the tunnel. For the larger 31.8 inch altitude the model travel was 16 inches, translating the model a distance of 4 orifices for each model position.

The reported linear actuator position is added to axially shift the pressure signature data to align each series of pressure signatures so that simple averaging of the data could be accomplished. Simply stated, an averaged signature, $\bar{f}$, is obtained by summing the signatures, f_i, at each port and dividing by N, the number of positions.

$$\bar{f} = \frac{\sum f_i}{N}$$

The mean signature is obtained at each port, where the shifted signatures overlap. Once the average value at each point is known, the standard deviation can be computed for each port.

$$\sigma = \sqrt{\frac{\sum (f_i - \bar{f})^2}{N}}$$

The average standard deviation along the rail serves as a figure of merit to determine the best reference run to use. When deciding which reference run to use in forming the spatially averaged signature, the one with the smallest average standard deviation over the entire signature is selected. Reference runs were taken before and after each series of data runs; usually the reference run *after* the data run offered less scatter. Often a reference run chosen this way for one series of data runs also turned out to be a more suitable reference run for another data run series. The choice of the reference run is important to the quality of the corrected signatures for the individual data runs at different tunnel positions, but is far less important to the quality of the spatially averaged signatures.

4.2 Total Pressure of 2300 psf

Operating the test slightly above atmospheric condition at a P_T of 2300 psf rather than 1450 psf as was used in tests since 2008 has significant advantages that outweigh the 10-15% increased power costs associated with the higher pressure. Listed below are some of the key reasons for running at 2300 psf:

- Higher Reynolds Number per foot (RN) of 4.43×10^6 compared with 2.88×10^6 at 1450 psf is obtained. Testing at a higher RN reduces the likelihood of flow separation from the model or blade mounting surfaces.

- Reduces the settling time of rail static pressures by nearly a factor of two
- Requires less dry (~50 ppm) high-pressure air to maintain humidity, and lower humidity levels are more easily obtained.
- Does not require test interruptions for re-pressurizing (vacuum state) external tanks (required when below atmosphere at 1450 psf); these interruptions took about 15-20 minutes every one to two hours.

4.3 Humidity

Maintaining a reasonably low humidity level was found to be very important. Higher levels of humidity cause rounding of the signatures and also cause spurious pressure signature data including shifts. After the first test in 2008, dry high-pressure air was pumped into the wind tunnel to reduce the humidity levels. Typically approximately 10 lbs/sec of dry air is pumped into the tunnel via a single pipe located under the strut just downstream of the test section. Stabilizing the humidity to within 4 ppm requires a significant amount of time, and significantly reduces test productivity.

4.4 Forward Rail Position

Testing with the RF 1.0 rail eliminates corruption of the pressure signatures caused by model shock reflections from the wall, and better data were obtained with the rail on the forward window blank of the test section than on the aft blank. The rail was on the forward blank for the T97-0231 test data shown in this report. The reason for the improved data in the forward tunnel position can only be determined by a detailed analysis of tunnel-empty flow field surveys. The model was positioned and translated upstream of the rail leading edge shock to eliminate the possibility of the rail shock waves and expansions affecting the model pressure signatures. CART3D-AERO computational results previously shown (Fig. 12) indicate some variation in pressure signature data with the model in the influence of the rail leading edge shock.

4.5 Sampling Time

The sampling time duration of the "data" runs (model pressures on rail) were typically 30 or 60 seconds and reference runs were usually 60-90 seconds, but with some 30 second runs. The 90 second duration was used because during previous tests it was the observed period of the tunnel total pressure variation, and taking the data over 90 seconds provided nearly the same average P_T between data and reference runs. However, during the T97-0231 test entry, the coarse pressure stabilization valve was fixed at a constant setting to reduce the pressure variation from 4 psf to less than 1 psf. The resulting period of pressure oscillation was only 5 seconds with the coarse valve fixed. The benefit of stabilizing the pressure could reduce the need for longer duration runs, but this conjecture needs study. Averaging the pressure signatures over a series of axial positions had the most benefit on the quality of the data. Data sampling duration has a strong influence on the quality of the individual data run but a small effect on the averaged signature. This is shown in Figures 19-21. Figure 19 shows the 26 pressure signatures for a run series (black lines), the averaged pressure signature (cyan), and one standard deviation from the averaged data (red) for the full 30-second

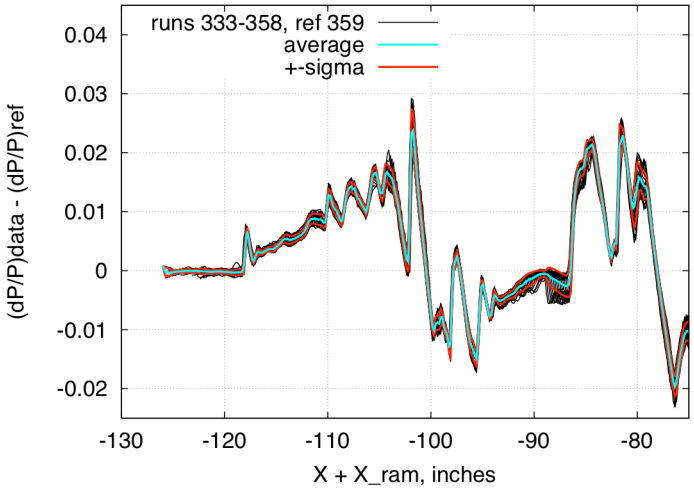

Figure 19: Experimental pressure signatures aligned by actuator position for runs 333-358, ref 359 with 30-second duration data.

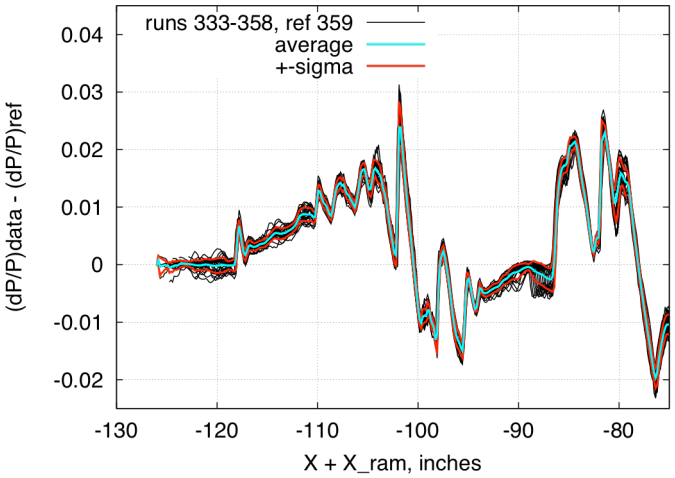

Figure 20: Experimental pressure signatures aligned by actuator position for runs 333-358, ref 359 with 2-second duration data run and 30-second reference run.

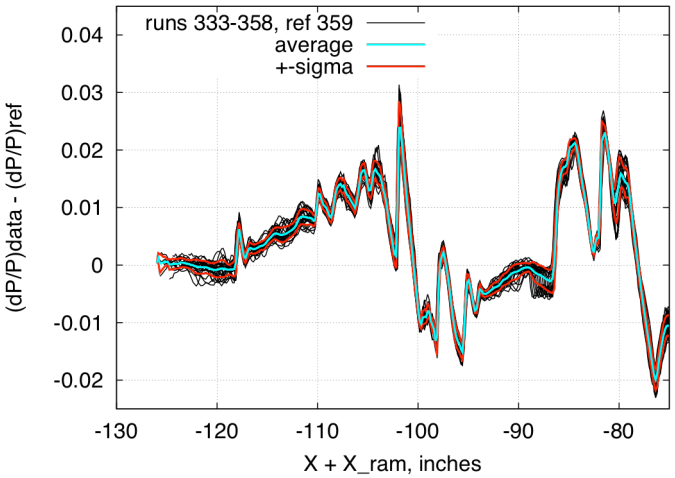

Figure 21: Experimental pressure signatures aligned by actuator position for runs 333-358, ref 359 with 2-second duration data.

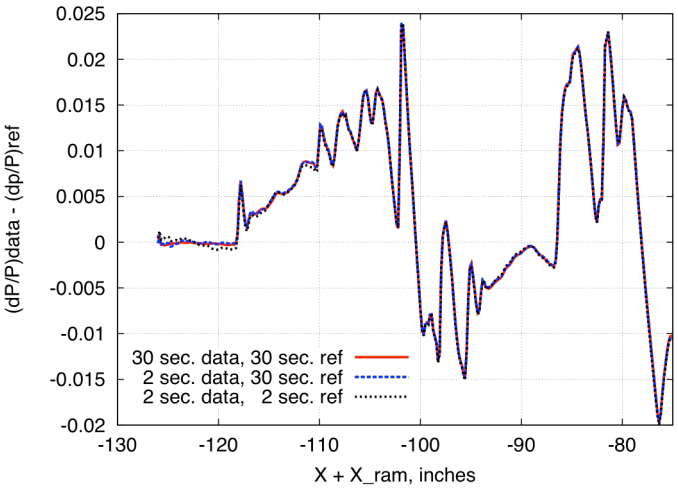

Figure 22: Averaged experimental pressure signatures comparing 30- and 2-second sampling time durations.

duration runs.

Figure 20 shows the test data runs with 2-second sampling times while using the 30-second reference run. Figure 21 shows data and reference runs both using 2-second sampling times. Comparing the variation of the individual signatures in Figs 19-21 it is clear that increasing the duration of the sampling time improves the quality of the temporal data. It appears advantageous to use a longer duration for the reference runs than for the data runs (compare Figs. 20 and 21). However, the averaged pressure signatures with the various sampling times show only small differences in the averaged data (Figure 22). There is almost no difference between the short duration data runs with the longer reference run compared to the longer duration data runs. This highlights a large potential savings in data acquisition time by shortening the sampling time for the overpressure runs in future tests.

5 Computational and Wind Tunnel Results

The Lockheed Martin Aeronautics Company's low sonic boom configuration, designed to meet NASA's stringent environmental targets and performance goals, was the primary configuration tested in the T97-0231 test. The N+2 aircraft configuration model and two axisymmetric calibration models were tested at Mach 1.6. A top blade mount to minimize the effect of the aft fuselage distortion on the pressure signature supported the aircraft model. A conventional sting that attached to the base of the model was also tested and compared with numerical simulations. Conventional sting support systems typically give questionable aft pressure signature data due to the additional aft fuselage volume required to attach a sting. Both the top blade and rear sting model supports were designed to hold the model at the design angle of attack so that the model remains equidistant from the RF 1.0 rail during axial translation in the tunnel. Computations of the Lockheed test configurations with both sting and blade mountings are compared to a simulation without the supports for an assessment of the flight vehicle and functionality of the supports.

5.1 Mesh Generation

The Mach Cone Aligned Prism (MCAP) method [12] was used with the AIRPLANE [21] and USM3D [22-23] flow solvers to accurately capture off-body sonic boom pressure signatures. Meshes were composed of dense near-field grids with cylindrically shaped boundaries encompassing the model just beyond its surface, and a MCAP mesh from the cylindrical boundary to the far field. The near-field grids were generated with MESH3D [24-26] for inviscid AIRPLANE computations, and TetRUSS [27] (GridTool and VGrid) software for viscous-flow computations with USM3D. The grid density was increased within the sonic boom zone of influence below the model to azimuthal angles of 90 degrees to accurately capture the sonic boom signature out to the cylindrical boundary. The inner cylindrical boundaries were then used as input to the MCAP software and projected in the radial direction and sheared to align with the Mach angle with a series of prism layers to the far field. The

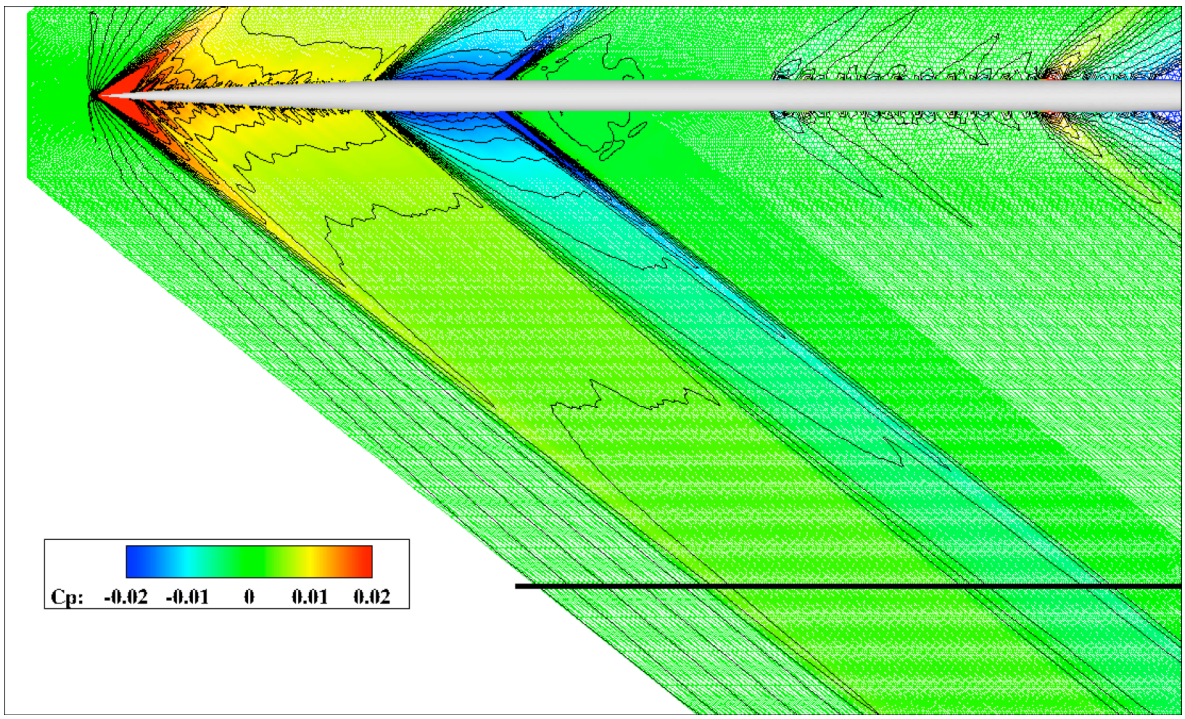

Figure 23: Symmetry plane grid colored by pressure coefficient and overlaid constant pressure lines for an AIRPLANE solution of the Seeb-ALR configuration, M=1.6, α=0.0 degrees. Signature sample line is shown 21.2 inches below the model.

prism structure retains the dense axial mesh and permits radial stretching with Mach cone alignment

around the aircraft model for accurate on- and off-track signatures in a robust manner without the possibility of crossed cells.

5.2 Axisymmetric Models

The axisymmetric calibration models are presented first. An AIRPLANE (Euler) computation of the Seeb-ALR model is shown with the symmetry plane solution at Mach 1.6, α= 0 degrees in Figure 23. The grid lines are colored by the coefficient of pressure, and black lines of constant pressure are overlaid. The horizontal line below the model identifies the location of the data sampling line 21.2 inches below the model. The non-aligned inner cylindrical mesh has mesh refinement within the sonic boom zone of influence, and that refinement continues to the outer boundary with the prism outer mesh. Shocks are aligned with the MCAP mesh near the configuration and at the location of the sampling line. Evidence of the alignment is seen by shocks parallel to the shear angle of the forward boundary. CART3D-AERO and AIRPLANE computations of the Seeb-ALR model are compared with experiment in Figure 24, where the experimental data presented are the average of a series of 25 runs at different axial tunnel positions. The bow shock and region of flat pressure is captured with both the Cartesian adapted and the MCAP tetrahedral computational methods.

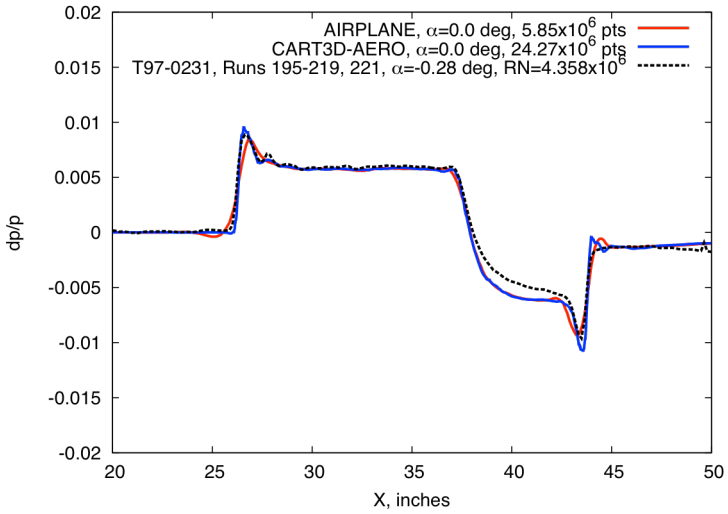

Figure 24: Seeb-ALR computations using AIRPLANE and CART3D-AERO compared with experiment, M=1.6, H=21.2 inches.

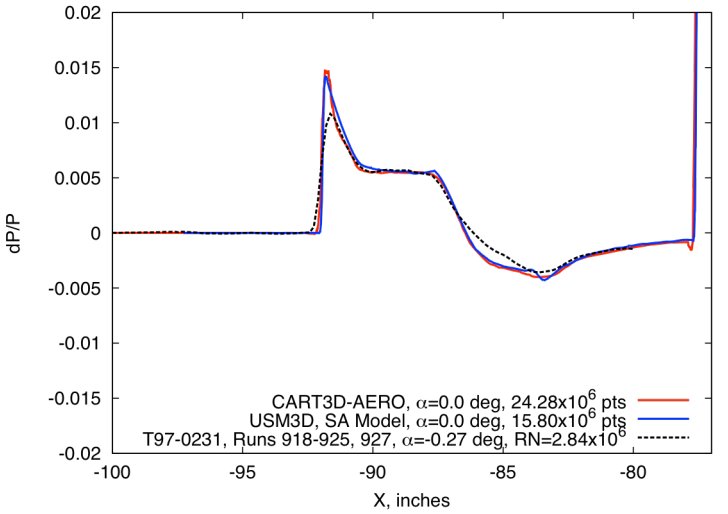

Figure 25: AS-2 computations using CART3D-AERO and USM3D (Navier-Stokes, RN=2.84x10^6 per foot) compared with experiment, M=1.6, H(CFD)=30.0 inches, H(Experiment) =31.8 inches.

The Boeing AS2 axisymmetric "Seeb" body was designed to produce a sonic boom pressure signature with a small 2-inch flat pressure region whereas the Lockheed Seeb-ALR was designed for an 8-inch flat region. CART3D-AERO and a viscous solution using USM3D with MCAP outer grids are compared with experiment in Figure 25. The experimental data shown are the average of only 8 experimental runs. The viscous computation was performed at the wind tunnel Reynolds number of 2.84×10^6 per foot using the Spalart-Allmaras turbulence model. The good agreement between the CART3D-AERO and USM3D results shows that the use of the Navier-Stokes equation was unnecessary at the low Reynolds number test condition. Experimental rounding of sharp

shocks is expected due to model vibration, rail orifice spacing, and averaging data with different stream angles and corresponding angle of attack differences.

5.3 Lockheed N+2 Model with Blade Mount

The Lockheed tri-jet model with the blade mount is shown installed in the 9x7 wind tunnel in Figure 26. The leading edge of the RF 1.0 rail and a small portion of the window blank are visible in the photograph. Viscous grids were developed for the wind tunnel Reynolds number of 4.33 million per foot for the Lockheed configuration with the blade mount. These grids and all other grids shown in this report utilized the MCAP methods to align the grids with the Mach cone. The USM3D solution on the symmetry plane is shown in Figure 27 for the test conditions shown in the figure caption. The symmetry plane grid is shown colored by pressure coefficient and overlaid

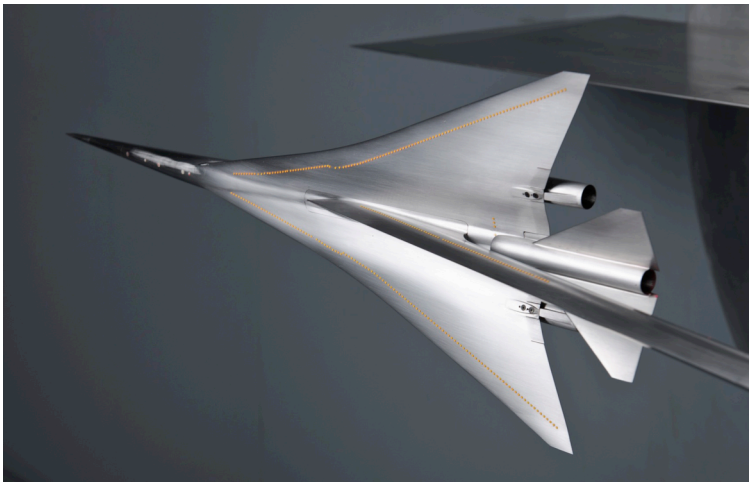

Figure 26: Installation photograph showing the Lockheed N+2 blade sting configuration and leading edge region of RF 1.0 rail.

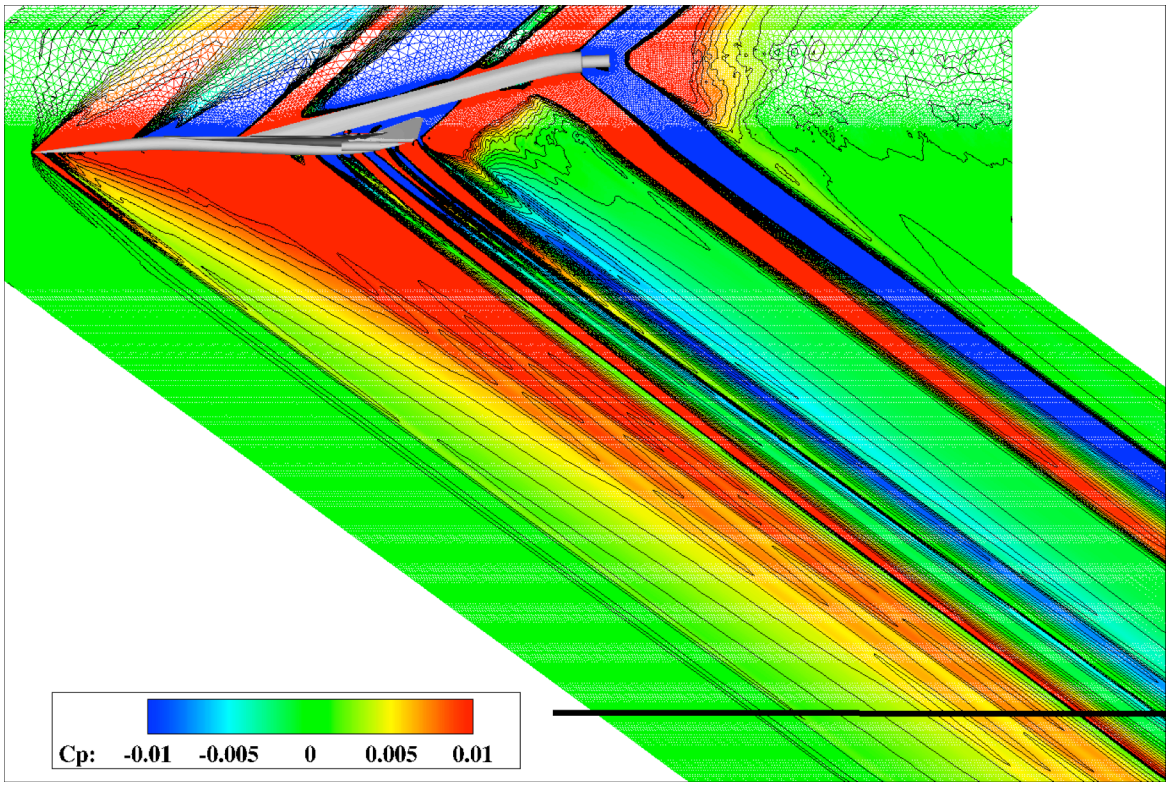

Figure 27: Mach cone aligned grid and solution with USM3D. Symmetry plane grid colored by pressure coefficient and overlaid lines of constant pressure; Signature sample line is 31.3 inches below the model. M=1.6, α=2.53 degrees, RN=4.3×10^6 per foot.

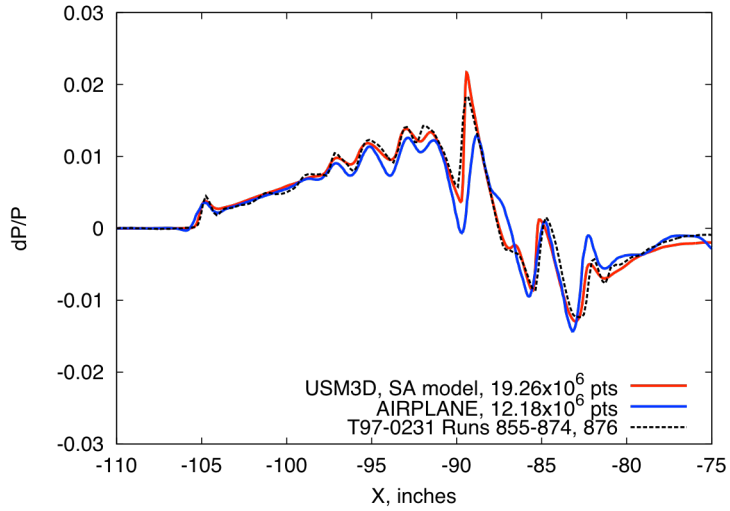

Figure 28: Lockheed N+2 blade mount configuration. USM3D (Navier Stokes), AIRPLANE (Euler) and Experiment, M=1.6, α=2.5 deg, H=31.3 inches, RN=4.3×10^6 per foot.

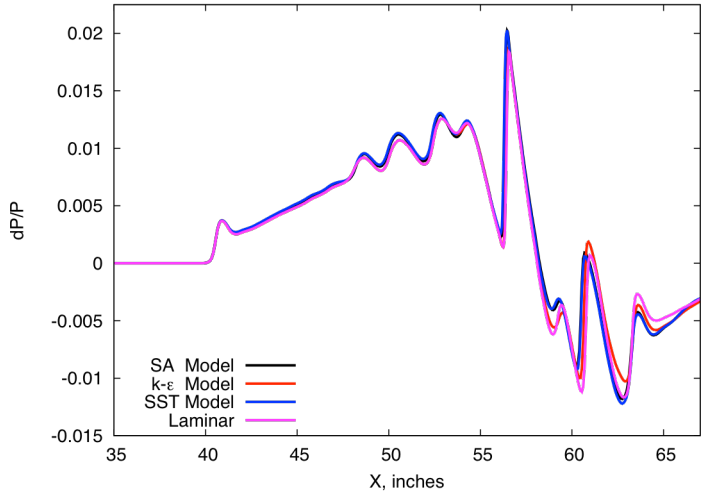

Figure 29: Effect of dissipation model on the LM N+2 with blade mount. M=1.6, H=31.5 inches, α=2.3 degrees.

with black lines of constant pressure. The grid is so dense that the individual triangular faces on the symmetry plane are not visible except above the model where dense grids are not necessary. The sampling line shown in the lower part of the figure indicates the location of the pressure rail relative to the model. The USM3D pressure signature shown in Figure 28 represents a turbulent flow solution using the Spalart-Allmaras turbulence model, and is compared with the RF 1.0 rail test data and an Euler solution obtained with AIRPLANE. The viscous solution shows excellent agreement with the data obtained with the RF 1.0 rail. The experimental data are plotted with a dashed line rather than symbols to clarify the details of the pressure signatures. The AIRPLANE inviscid computation shows discrepancies in the vicinity of the peak overpressure region of the pressure signature. The peak overpressure emanates from near the wing trailing edge and the flow is complicated by the presence of the blade, top mounted nacelle and the close proximity of the tail. The difference between the Euler and Navier-Stokes computations show the importance of modeling the boundary layer for this model. The discrepancies between the Euler and low Reynolds number data are similar to an angle of attack or lift coefficient effect [10]. The Euler solution may be a more realistic result for the flight Reynolds number of the vehicle. The flight Reynolds number is 2.0×10^6 per foot for a 50,000 foot flight altitude at Mach 1.7.

USM3D computations were obtained at an angle of attack of 2.3 degrees for the Spalart-Allmaras (SA), K-epsilon (k-ε), and Menter's shear stress transport (SST) K-omega (k-ω) turbulence models, and a laminar flow solution. There was little difference in the pressure signatures obtained with the SA and SST models and only slight differences are seen with the k-ε and the laminar solution (Figure 29). Small trip disks were attached near the model's wing leading edge, blade mount, and also on wing upstream of shock impingement from the nacelles to energize the boundary layer to reduce the possibility of flow separation, rather than trip the boundary layer. The laminar solution would be expected to be less representative of the flow than the turbulent solutions because of the trip disks.

These small trips were not modeled in any of the computations, and the effect on pressure signature was not evaluated experimentally; the trip disks remained affixed to the model for the entire wind tunnel test. As a result of the excellent agreement between the experimental results and computations with the SA model, and the small effect of turbulence model, all the remaining computations will use the SA turbulence model.

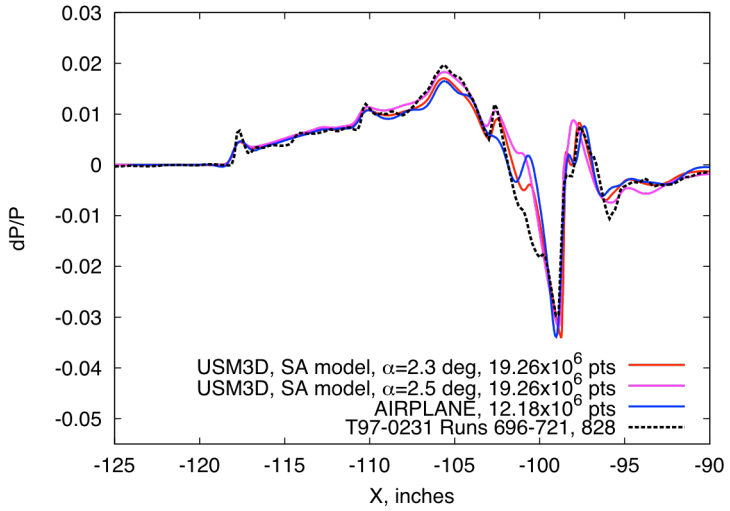

Figure 30: Lockheed N+2 blade mount configuration. USM3D (Navier Stokes), AIRPLANE (Euler) and Experiment. Off-track results, ϕ=40 deg, M=1.6, α=2.5 deg, H=20.8 inches, RN=4.3×10^6 per foot.

Off-track computations at an azimuthal angle of 40 degrees are compared with experiment in Figure 30. The reduced wing shock and increased tail shock strength occurring off-track compared with the previous on-track results are predicted by both the inviscid and viscous computations. Overall, the computational results compare fairly well with experiment but not as well as the on-track comparisons. Differences between the computational and physical model may cause these discrepancies.

5.4 Lockheed N+2 Model with Conventional Sting

The Lockheed N+2 model attached to the conventional sting is shown in a photograph of the lower surface with oil flow (Figure 31). The colored oil was used to identify attached and separated flow regions during and after testing. Boundary layer trip disks were applied to the upper and lower surfaces of the model to energize the boundary layer rather than cause transition and were thought to be effective in keeping the flow attached everywhere except on portions of the blade mount and in the regions of influence of the nacelle pylon shocks. The trip disks were applied to the vehicle for the entire test, but not modeled in the computations. The computations with the conventional sting are compared with on- and off-track experiment in Figures 32 and 33. The USM3D computations again provide better correlation with experiment than the inviscid AIRPLANE computations as expected. These computations corroborate the experimental results with the RF 1.0 rail.

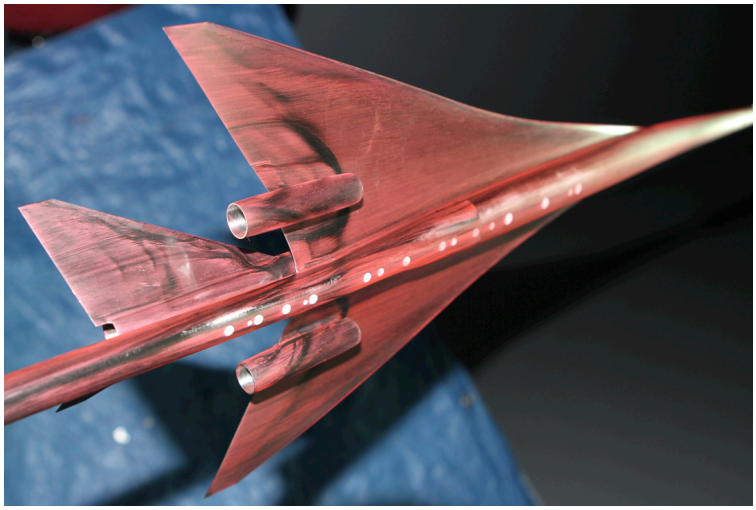

Figure 31: Lockheed N+2 with conventional sting. Photograph shows oil flow on underside of model.

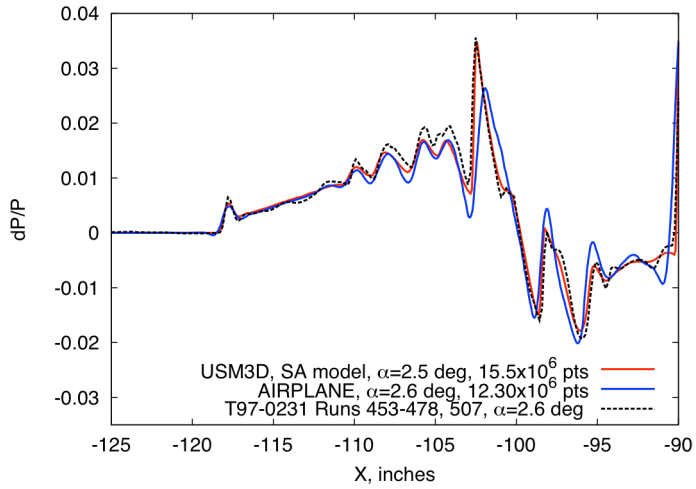

Figure 32: Lockheed N+2 conventional sting, USM3D (Navier Stokes), AIRPLANE (Euler) and Experiment, M=1.6, α=2.6 deg, H=21.1 inches, RN=4.3×10^6 per foot.

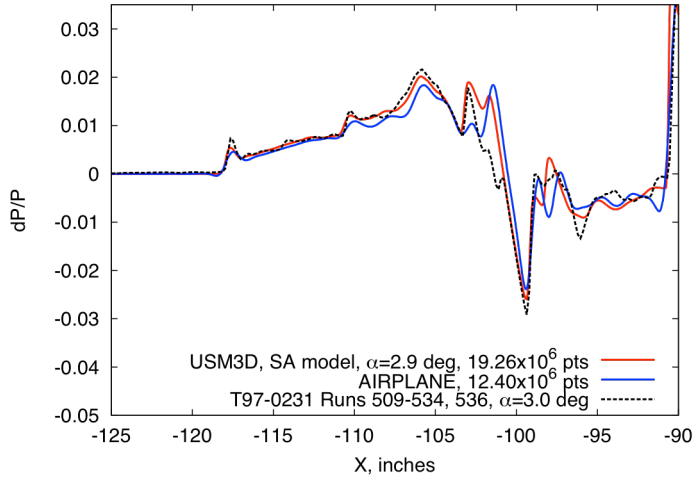

Figure 33: Lockheed N+2 conventional sting, USM3D (Navier Stokes), AIRPLANE (Euler) and experiment. Off-track results, ϕ=40 deg, M=1.6, α=2.9 deg, H=21.2 inches, RN=4.3×10^6 per foot.

5.5 Lockheed "Flight Vehicle"

USM3D computations were performed at the design angle of attack of 2.3 degrees for the model with sting and blade mountings, and without model support (Figure 34). The blade component was removed from the blade-mounted model to obtain a "flight vehicle" configuration. The sting- and blade-mounted models compared to a simulated "flight vehicle" are shown at the experimental Reynolds number. These on-track computations show the effectiveness of the blade mount; the pressure signature of the model with the blade-mount is nearly identical to the model without model support, whereas the pressure signature of the model with the conventional sting does not correlate well with experimental data particularly in the wing shock and expansion regions.

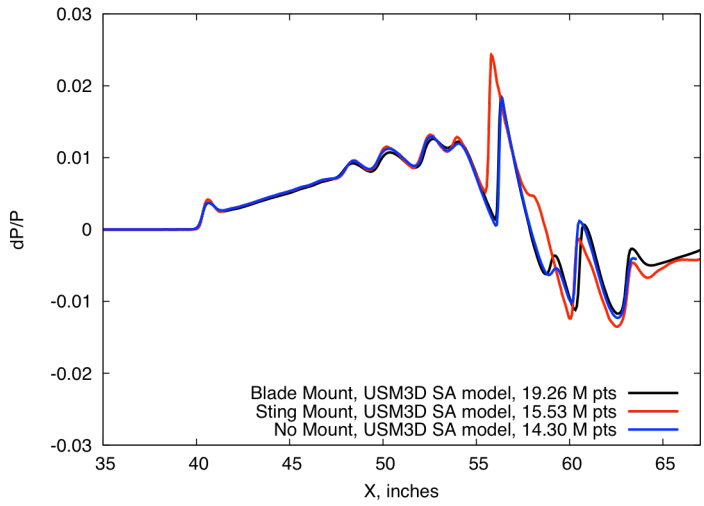

Figure 34: Lockheed N+2 with sting and blade-mount compared with "flight vehicle" concept (no mount). USM3D (Navier Stokes) M=1.6, α=2.3 deg, H=31.3 inches, RN=4.3×10^6 per foot.

6 Summary

The use of the RF 1.0 rail combined with spatial averaging of aligned signatures with different axial positions and constant altitude eliminated the wind tunnel distortions seen in the individual pressure signatures at most fixed model positions in the wind tunnel. The rail data were, as predicted, free from model shock reflections and required no scaling. The data from this test proved that accurate data with reasonable acquisition time is obtainable in the Ames 9- by 7-Foot Supersonic Wind Tunnel.

The adjoint-based mesh adaptation method, CART3D-AERO, was used to validate the RF 1.0 pressure rail. This was accomplished by obtaining accurate solutions along line sensors above the tip of the RF 1.0 rail for combinations of model, rail, and wind tunnel wall. The highly accurate results of the CART3D-AERO computations compared to free-air solutions of the models allowed predictions of the experimental pressure signatures on the rail. The computational results correctly predicted the effects of models in the influence of the rail leading edge compression region, and the expected effect of a small cross flow change in the wind tunnel. Without this highly effective and easy to use method it is likely that this new pressure rail would not have come to fruition.

The computed pressure signatures from the tetrahedral mesh methods (USM3D and AIRPLANE) using stretched Mach cone aligned prism cells closely matched the experimental pressures obtained with the RF 1.0 rail.

Substantial productivity gains can be obtained in future wind tunnel tests by decreasing the duration of the sampling time of the data runs at each model position in the tunnel. Data runs with 2-second duration acquisition times are of the same accuracy as 30-second duration times when a series of data runs are averaged. However, the individual data runs at different axial positions will be of lower quality with reduced duration.

The new highly accurate sonic boom pressure data from recent tests will aid in the development of improved computational and grid generation techniques for sonic boom analysis in the future by providing the data and model geometries to the aircraft industries for study.

Acknowledgments

The authors would like to thank Michael Buonanno, Robert Langberg, and Nicole Norstrud from Lockheed Martin Aeronautics; Todd Magee and Eric Adamson from The Boeing Company; Marian Nemec, Scott Murman, Maureen Delgado, and Bruce Storms from Ames Research Center; Peter Coen, Linda Bangert, Ed Parlette, Eric Walker, Richard Campbell, and Mohagna Pandya from Langley Research Center, and Clayton Meyers from Glenn Research Center.

References

[1] M. Nemec, M. Aftosmis, and M. Wintzer, "Adjoint-based Adaptive Mesh Refinement for Complex Geometries," *AIAA Paper 2008-0725*, January 2008

[2] Jones, W.T., Nielsen, E. J., and Park M. A., "Validation of 3D Adjoint Based Error Estimation and Mesh Adaption for Sonic Boom Prediction," *AIAA Paper 2006-1150*, 44th AIAA Aerospace Sciences Meeting and Exhibit, Reno, NV, January 2006.

[3] Lee-Rausch, E. M., Park M. A., Jones, W. T., Hammond, D. P., and Nielsen, E. J., "Application of a Parallel Adjoint-based Error Estimation and Anisotropic Grid Adaption for Three-dimensional Aerospace Configurations," *AIAA Paper 2005-4842*, 2005.

[4] Carter, Melissa B., and Deere, Karen A., "Grid Sourcing and Adaptation Study Using Unstructured Grids for Supersonic Boom Prediction," *AIAA Paper 2008-6595*, 2008.

[5] Aftosmis, M. J., and Berger, M. J., "Multilevel Error Estimation and Adaptive H-Refinement for Cartesian meshes with embedded boundaries," *AIAA Paper 2002-0863*, 40th AIAA Aerospace Sciences Meeting and Exhibit, Reno NV, Jan. 2002.

[6] Nemec, M., and Aftosmis, M., "Adjoint Error-Estimation and Adaptive Refinement for Embedded-Boundary Cartesian Meshes," *AIAA Paper 2007-4187*, 18th AIAA CFD Conference, Miami FL, June 2007.

[7] Wintzer, M., Nemec, M., and Aftosmis, M. J., "Adjoint-based Adaptive Mesh Refinement for Sonic Boom Prediction," *AIAA Paper 2008-6593*, 26th AIAA Applied Aerodynamics Conference, Honolulu HI, June 2008.

[8] Choi, S., Alonso, J. J., and Van der Weide, E., "Numerical and Mesh Resolution Requirements for Accurate Sonic Boom Prediction," *AIAA Journal of Aircraft,* Vol. 46, No. 4, July-Aug. 2009.

[9] Cliff, S., Thomas, S., McMullen, M., Melton, J., and Durston, D., "Assessment of Unstructured Euler Methods for Sonic Boom Pressure Signatures Using Grid Refinement and Domain Rotation," *NASA/TM-2008-214568*, Sept. 2008.

[10] S. Cliff, A. Elmiligui, R. Campbell, and S. Thomas, "Evaluation of Refined Tetrahedral Meshes with Projected, Stretched and Sheared Prism Layers for Sonic Boom Analysis," AIAA Paper 2011-3338, June 2011.

[11] Campbell, R. L., Carter, M. B., Deere, K. A. and Waithe, K. A., "Efficient Unstructured Grid Adaptation Methods for Sonic Boom Prediction," *AIAA Paper-7327*, Honolulu HI, Aug. 2008.

[12] Cliff, S.E., Elmiligui, A. A.,Campbell, R. L., and Thomas, S. D., "Evaluation of Refined Tetrahedral Mesh with Projected, Stretched, and Sheared Prism Layers for Sonic Boom analysis, AIAA-2011-3338, Honolulu, HI, June 2011.

[13] Durston, D. A., Cliff, S. E., Wayman, T., Merret J., Elmiligui, A., and Bangert, L., "Near-Field Sonic Boom Test on Two Low-Boom Configurations Using Multiple Measurement Techniques at NASA Ames," AIAA-2011-3333, Honolulu, HI, June 2011.

[14] Morgenstern, J.M., Buonanno, M., and Norstrud, N., "N+2 Low Boom Wind Tunnel Model

Design and Validation," AIAA-2012-3217, 33rd Applied Aerodynamics Conference, June 2012.

[15] Aftosmis, M. J., Nemec, M., and Cliff, S.E., "Adjoint-Based Low-Boom Design with Cart3D," AIAA-2011-3500, Honolulu, HI, June 2011.

[16] Darden, C. M., "Sonic Boom Minimization with Nose-Bluntness," NASA TP 1348, 1979.

[17] George, A. R., and Seebass, R., "Sonic Boom Minimization Including Both Front and Rear Shocks," AIAA J. Vol. 9, No. 10, Oct. 1971, pp. 2091-2903.

[18] Heineck, J. T., Schairer, E. T., Walker, L. A., Kusher L. K., "Retroreflective Background Oriented Schlieren (RBOS)," ISV14-14-14th International Symposium on Flow Visualization, EXCO Daegu, Korea, June, 2010.

[19] Morgenstern, J.M., "Distortion Correction for Low Sonic Boom Measurement in Wind Tunnels," AIAA-2012-3216, 33rd Applied Aerodynamics Conference, June 2012.

[20] Morgenstern, J.M., "How to Accurately Measure Low Sonic Boom or Model Surface Pressures in Supersonic Wind Tunnels," AIAA-2012-3215, 33rd Applied Aerodynamics Conference, June 2012.

[21] Jameson, A., and Baker, T., "Improvements to the Aircraft Euler Method," *AIAA Paper-87-0452*, 1987.

[22] Frink, N. T., Pirzadeh, S. Z., Parikh, P. C., Pandya, M. J., and Bhat, M. K., "The NASA Tetrahedral Unstructured Software System," *The Aeronautical Journal*, Vol. 104, No. 1040, October 2000, pp. 491-499.

[23] Frink, N. T., "Assessment of an Unstructured-Grid Method for Predicting 3-D Turbulent Viscous Flows," *AIAA Paper-96-0292*, Jan. 1996.

[24] Baker, T. J., "Generation of Tetrahedral Meshes around Complete Aircraft," Second International Conf. on Numerical Grid Generation in Computational Fluid Dynamics, NASA and Airforce Office of Scientific Research, Miami Beach, FL, Dec. 1988.

[25] Baker, T. J., "Automatic Mesh Generation for Complex Three-Dimensional Regions Using a Constrained Delaunay Triangulation," Engineering with Computers, vol. 5, nos. 3 and 4, 1989.

[26] Baker, T. J., and Vassberg, J. C., "Tetrahedral Mesh Generation and Optimization," Proc. Of the 6th International Conf. on Numerical Grid Generation, Greenwich, UK, July 1998, pp. 337-349.

[27] Pirzadeh, S., "Advanced Unstructured Grid Generation for Challenging Aerodynamics Applications," *AIAA Paper 2008-7178*, Aug. 2008